FEATURE ARTICLE

Thermal Characterization and Sensor Applications of One-Dimensional Nanostructures Employing Microelectromechanical Systems

Li Shi,* Choongho Yu, and Jianhua Zhou

Department of Mechanical Engineering & Center for Nano- and Molecular Science and Technology, Texas Materials Institute, The University of Texas at Austin, Austin, Texas 78712

Received: July 15, 2005

We review the recent progress in thermal characterization and sensor applications of one-dimensional nanostructures employing microelectromechanical system (MEMS) devices. It was found by thermal measurements that the thermal conductance of a single wall carbon nanotube (SWCNT) was very close to the ballistic thermal conductance of a 1-nm-diameter SWCNT without signatures of phonon−phonon Umklapp scattering, a high thermoelectric figure of merit can potentially be obtained in bismuth telluride ($Bi_xTe_{1−x}$) nanowires with an optimized atomic ratio of x, and the thermal conductivity of metal oxide nanobelts was suppressed by increased phonon-boundary scattering. We further suggest that dielectrophoresis and other directed-assembly methods can be used for the large-scale integration of nanowires with MEMS to obtain ultrasensitive, stable, and selective sensor systems.

I. Introduction

One-dimensional (1D) nanostructures such as carbon nanotubes[1] and semiconductor nanowires[2] have received intense interest in recent years. These nanostructures have been obtained using either new "bottom-up" synthetic methods or state-of-the-art nanolithography-based patterning approaches. There have been a large number of efforts to employ these nanostructures for the fabrication of field effect transistors,[3−6] logic devices,[7,8] solid-state lasers,[9] gas and biomolecular sensors,[10,11] field emission displays,[12−14] and thermoelectric refrigeration and power generation devices.[15] These many potential applications are accompanied by new challenges, one of which is related to the unique thermal and thermoelectric transport properties of nanotubes and nanowires. In bulk materials, thermal energy transport is facilitated by lattice vibration waves or phonons as well as charge carriers. Consequently, the thermal conductivity (κ), which is the proportionality factor between temperature gradient and heat flux, consists of a phonon contribution (κ_p) and an electron contribution (κ_e), i.e., $\kappa = \kappa_p + \kappa_e$. In metals, κ_e is much larger than κ_p; while in insulators and semiconductors, κ_p is much larger than κ_e. κ_p (or κ_e) is determined by the energy dispersion and scattering processes of phonons (or electrons), both of which can be modified in nanostructures due to size and quantum confinements. It was suggested that the κ_p of semiconductor nanowires can be largely suppressed by increased surface scattering of phonons[16] and by modification of the phonon energy dispersion.[17] The suppressed κ_p makes it difficult for Joule heat generated locally in nanowire electronic devices to be dissipated to the substrate, leading to local hot spots that degrade the device performance and reliability.

The self-heating problem has been one of the major challenges for continuous scaling down of metal-oxide field-effect-transistor (MOSFET) devices in ultra-large-scale-integrated (ULSI) circuits,[18] and will likely become one critical issue for the development of nanotube and nanowire electronic devices, especially those on flexible, low-cost polymer substrates with thermal conductivity two or more orders of magnitude lower than silicon. Thermal management is an increasingly important aspect for the further development of nanoelectronics.

One approach to address the thermal management problem relies on the development of high-thermal conductivity materials to act as heat spreaders in electronic packaging. Good-quality diamond has been known as an excellent heat conductor with a high thermal conductivity up to 3000 W/m-K at temperature 300 K, compared to the corresponding value of 400 W/m−K for copper, 150 W/m-K for silicon, 1.4 W/m-K for glass, and 0.1 W/m-K or lower for polymers. Diamond coating deposited by chemical vapor deposition (CVD) has been explored as heat spreading coating for ULSI devices,[18,19] although the difficulty and cost for the synthesis of high-quality diamond has limited its application. The discovery of carbon nanotubes (CNTs) provides a different type of high-thermal conductivity materials for thermal management applications. Unlike semiconductor nanowires, CNTs are expected to possess super-high κ due to its unique crystalline structure, low defect concentrations, and atomically smooth surface. Various theoretical calculations have predicted that κ of carbon nanotubes (CNTs) can surpass that of diamond.[20,21] The predictions have inspired the active development of CNT films and composites for applications as thermal interface materials for reducing the thermal interface resistance in electronic packaging. Additionally, CNT interconnect structures are also being actively pursued for next-generation ULSI devices.[22,23] If successful, CNT interconnects especially CNT via structures not only can support a large current density but they also can be used as heat spreaders to dissipate heat from local hot spots.

On the other hand, the suppressed κ in semiconductor nanowires can be advantageous to the fabrication of energy-

---

* Corresponding author. E-mail: lishi@mail.utexas.edu.

Li Shi is an assistant professor in the Department of Mechanical Engineering and Texas Materials Institute at the University of Texas at Austin (UT Austin). He received his B. S. from Tsinghua University, Beijing, in 1991, his M.S. from Arizona State University, Tempe, in 1997, and his Ph.D. from the University of California at Berkeley in 2001. He was a Research Staff Member at IBM Research Division for one year before joining the faculty at UT Austin in 2002. He received the CAREER award from the National Science Foundation in 2003 and the Young Investigator Award from the Office of Naval Research in 2004. Current research undertaken by his group includes nanostructured thermoelectric materials, fundamentals of nanoscale energy transport and conversion, nanosensors, MEMS and microfluidics, and nanoscale interconnect structures for microelectronics.

Choongho Yu received his B.S. and M.S. degrees from Korea University and his Ph.D. degree in mechanical engineering from the University of Texas at Austin in 2004. He is currently a Postdoctoral Fellow at Lawrence Berkeley National Laboratory. His research interests include the investigation of thermoelectric materials for efficient power generation and refrigeration, thermophysical properties of low-dimensional nanostructures, and the development of molecular sensors and bio-MEMS.

Jianhua Zhou received his Ph.D. degree in mechanical engineering from the University of Texas at Austin in 2005. His research topic is in the area of thermal and thermoelectric transport in nanostructured materials. He obtained his B.S. and M.S. degrees, both in thermal engineering, from Tsinghua University in 1990 and 2000, respectively. He was a mechanical engineer at Nanjing Turbine Works from 1990 to 1997. He is currently with Applied Materials, Inc.

efficient thermoelectric (TE) refrigeration devices for thermal management applications. TE refrigeration is achieved by the Peltier effect, whereby a current flow across thermocouple junctions can produce cooling or heating. Conversely, a temperature difference across a TE material generates a current flow and thereby electrical power, allowing for direct thermal-to-electrical energy conversion.[24,25] Compared to vapor-compression refrigerators and gas-based engines, such solid-state devices are extremely attractive because they do not contain any moving parts, are environmentally benign, and allow for miniaturization. However, the coefficient of performance (COP) for TE refrigeration and the efficiency for TE power generation have been limited by the low TE figures of merit of bulk materials and are inferior to systems based on a working fluid.

The dimensionless TE figure of merit is defined as $ZT \equiv S^2\sigma T/\kappa$, where S is the Seebeck coefficient, σ is the electrical conductivity, κ is the thermal conductivity, and T is the temperature. A ZT larger than 3 is needed for a TE refrigeration unit to obtain a COP comparable to that of a vapor compression unit; while a ZT larger than 6 is required to increase the efficiency of a TE generator to 20%. During the past fifty years, bismuth telluride alloys, e.g. $Bi_{0.5}Sb_{1.5}Te_3$ with a ZT value approaching unity at 300 K, have remained the bulk materials with the highest ZT at room temperature. Increasing the ZT of bulk materials beyond this value has proved to be difficult due to two factors: (i) there is a tradeoff between S and σ as the dopant concentration is varied; and (ii) κ_e is proportional to σ according to the Wiedemann−Franz law.

Advances in nanostructured materials have led to new approaches to increasing the ZT. Theoretical calculations have suggested that $S^2\sigma$ can be increased in dimension-confined nanostructures due to a high density of states near the Fermi level,[26,27] and κ can be largely suppressed by phonon-boundary scattering[28] and possibly by modification of phonon dispersion. Recently, there have been reports on the growth of thin film superlattices[29,30] and nanostructured bulk alloys[31] with improved

ZT. Due to the quantum and classical size confinement effects, very high ZT values have been predicted in Bi-based[32] and III−V[33] nanowires.

There have been efforts to experimentally verify the super-high κ of CNTs, suppressed κ in semiconductor nanowires and ZT enhancement in bismuth-based and III−V nanowires. The thermal conductivity of SWCNT mats and bundles was measured.[34−36] The reported κ values are one or two orders of magnitude lower than theoretical calculations because the thermal resistance of the sample was increased by thermal contact resistance between interconnected CNTs in the sample. Measurement results of S and the electrical resistance (R) of bismuth[37] and bismuth antimony[38] nanowire arrays deposited in anodized alumina membranes (AAMs) have been reported, but the thermal conductivity was not obtained due to thermal leakage through the AAM. Thermal conductivity measurements of 1D nanostructures are challenging due to the small sample dimension.

A so-called 3-ω method has been employed to measure the thermal conductivity of a platinum wire, a large MWCNT bundle,[39] and recently an individual MWCNT.[40] This method relies on self-heating of a suspended wire under a sinusoidal current ($i_0 \sin\omega t$) of frequency ω. The sinusoidal current leads to a temperature rise modulated at the second harmonic frequency (2ω). Due to the temperature-dependence of the electrical resistance (R) of the wire, R is also modulated at the 2ω frequency. The voltage drop along the wire is $v = R(i_0\sin\omega t)$ and contains a modulated component ($v_{3\omega}$) at the 3ω frequency. The thermal conductivity of the wire is obtained with the use of a well-defined correlation between $v_{3\omega}$ and the thermal conductivity in the low-frequency regime. For using this method to measure a nanowire, however, it is important that the nanowire is metallic with a large temperature coefficient of resistance (TCR). Additionally, the contact electrical resistance needs to be eliminated so that the electrical resistance of the nanowire can be obtained. In four-probe measurements of the electrical resistance of very fine nanowires or nanotubes with the diameter on the order of 1 nm, however, the mesoscopic voltage probes are often invasive and can very well be the dominant source of scattering and hence resistance.[41] Unless very weakly coupling or noninvasive voltage probes are used in the four probe measurement, the obtained four-probe resistance is not purely the intrinsic resistance of the nanostructure and cannot be used to obtain the temperature rise in the nanostructure. Moreover, electrons and phonons need to be at equilibrium during self-heating so that resistance thermometry can be employed. In SWCNTs and other nanowires under self-heating in a high electric field, electrons and phonons are not necessarily at equilibrium because the length of the nanostructure is comparable to the mean free paths for scattering between these carriers. This issue is often the case at low temperatures, where the mean free path can be long. Consequently, the 3ω self-heating method cannot be applied to obtain the temperature-dependent thermal properties of these nanostructures.

Recently, we have developed a method to characterize the thermal and thermoelectric properties of individual nanotubes and nanowires with the use of microelectromechanical systems (MEMS) devices.[36] We have investigated several methods for the effective assembly of 1D nanostructures with the MEMS device. The successful integration of nanowires with MEMS not only allows us to characterize nanowire properties but also enables the integration of "bottom-up" synthesized nanowires with "top-down" patterned and etched microsystems for the large-scale fabrication of functional nanowire devices. Based
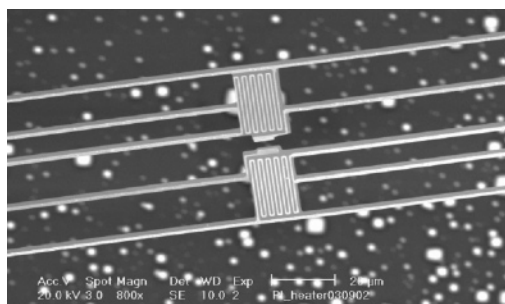
Figure 1. Scanning electron microscopy (SEM) image of the MEMS device for thermal characterization of 1D nanostructures. Reproduced with permission from ref 49. Copyright 2005 American Chemical Society.

on this approach, we have demonstrated highly sensitive and stable nanowire sensors.[42]

The following section discusses the experimental method, our recent measurement results of thermal and thermoelectric properties of single wall (SW) CNTs, semiconductor nanowires, and metal oxide nanobelts, and the integration of metal oxide nanobelts with MEMS for sensor applications.

II. Experimental Methods

Assembly of Nanowires with MEMS. Figure 1 shows a scanning electron micrograph (SEM) of the microdevice for nanowire characterization. The device was fabricated with the use of MEMS fabrication technologies. About 2000 devices can be fabricated on a 100-mm-diameter silicon wafer. The device consisted of two adjacent 14 μm × 25 μm low-stress silicon nitride (SiN$_x$) membranes, each suspended with five 0.5-μm-thick, 420-μm-long, and 2-μm-wide SiN$_x$ beams. One 30-nm-thick and 300-nm-wide platinum resistance thermometer (PRT) serpentine was patterned on each membrane. The PRT was connected to 200 μm × 200 μm Pt bonding pads on the substrate via 1.8-μm-wide Pt leads on the long SiN$_x$ beams. An additional 1.8-μm-wide Pt electrode was patterned on each membrane next to each other.

The nanowire sample can be trapped on the two Pt electrodes with the use of a wet deposition method. In this method, a drop of the nanowire suspension was deposited on a diced wafer piece that contained fourteen densely packed membrane structures. The wafer piece covered by the solution was rocked to induce a fluid motion in a direction perpendicular to the parallel electrode pair on the membranes. Aligned by the fluid motion, nanowires often crossed the two closely spaced Pt electrodes after the solution was dried uniformly on the wafer, while no nanowires were left bridging the long SiN$_x$ beams that were far apart from each other. Figure 2 shows a bismuth telluride (Bi$_x$Te$_{1-x}$) nanowire trapped on the two membranes of the microdevice with the use of this method.

To increase the assembly yield, we have investigated an electric field-directed assembly method. In this method, the two Pt electrodes in the microdevice were connected to an alternating current (AC) voltage source. As a solution containing the nanowires was dispersed on the wafer surface, the frequency of the AC voltage was adjusted to generate an attractive force on the nanowires that were polarized in the nonuniform AC electric field. This phenomenon is called positive dielectrophoresis, where a polarizable particle in a nonuniform AC electric field is attracted to regions of high field strength.[43] The attractive or positive dielectrophoretic force can be used to align and trap a nanowire onto the two Pt electrodes. We found that the suitable frequency and root-mean-square (rms) amplitude of the AC voltage were about 1 × 10^6 Hz and 5 V, respectively,
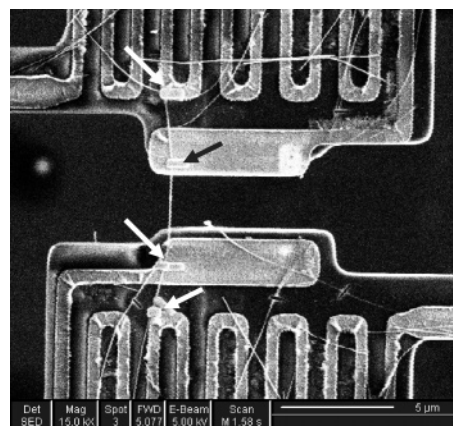

Figure 2. SEM image of a Bi$_x$Te$_{1-x}$ nanowire trapped between the two suspended membranes of the microdevice. The arrows indicate four short Pt lines deposited on the nanowire by a focused ion beam (FIB) deposition method. Reproduced with permission from ref 53. Copyright 2005 American Institute of Physics.
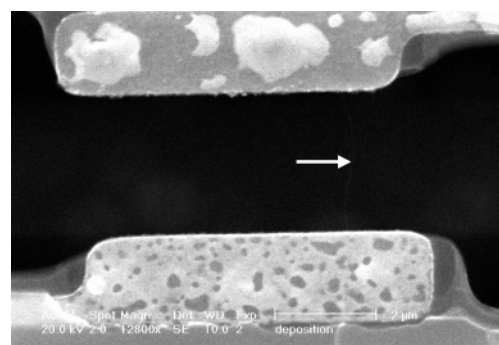

Figure 3. SEM image showing a suspended SWCNT (indicated by the arrow) grown between the two Pt electrodes of the microdevice. Reproduced with permission from ref 49. Copyright 2005 American Chemical Society.

for trapping tin dioxide (SnO$_2$) nanobelts. Similar methods have been reported for trapping nanotubes[44] and nanowires[45,46] with a yield approaching 100%.

Additionally, we have used a chemical vapor deposition (CVD) method to grow individual SWCNTs bridging the two membranes of the microdevice. A solution containing catalyst made of Fe, Mo and Al$_2$O$_3$ nanoparticles was spun on the suspended membranes, leaving catalyst particles on the membrane after the solution was dried. Alternatively, a sharp probe was used to deliver catalyst nanoparticles directly onto the two membranes. The suspended device was loaded in a 900 °C CVD tube furnace with flowing methane,[47] yielding individual SWCNTs grown between two catalyst particles on the two Pt electrodes. Figure 3 shows a SWCNT grown by this method.

Thermal Conductance Measurement. The measurement device was placed in an evacuated cryostat. With a direct current (I) flowing to one of the two PRTs, Joule heat in the amount of $Q_h = I^2 R_h$ was generated in this heating PRT with a resistance of R_h. Joule heat in the amount of $2Q_L = 2I^2 R_L$ was generated in the two Pt leads supplying the heating current to the PRT, where R_L is the resistance of one Pt lead. Some of the heat (Q_2) is conducted through the sample from the heating membrane to the other membrane, which is denoted as the sensing membrane, and raised the temperature of the latter by ΔT_s. In vacuum and with a small temperature rise on the heating membrane, ΔT_h, heat transfer by radiation and air conduction is negligible compared to Q_2. The temperature distribution in each membrane is uniform, and the maximum temperature
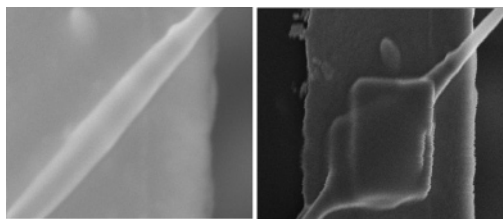
Figure 4. SEM images showing a Pt layer deposited on the contact between a carbon nanofiber and a Pt electrode on the suspended device with the use of focused electron beam deposition (left) and focused ion beam deposition (right).

difference in the heating (or sensing) membrane was calculated to be 1.8% (or 3.1%) of the temperature rise in the membrane.[48]

The total thermal conductance of the five identical supporting beams can be calculated as $G_b = 5\kappa_l A/L$, where κ_l, A, and L are the thermal conductivity, cross sectional area, and length of each beam, respectively. It can be shown that

$$G_b = \frac{Q_h + Q_L}{\Delta T_h + \Delta T_s} \qquad (1a)$$

The thermal conductance of the sample is obtained as

$$G_s = G_b \frac{\Delta T_s}{\Delta T_h - \Delta T_s} \qquad (1b)$$

Reduction of the Thermal Contact Resistance. The measured thermal resistance of the sample ($R_m = G_m^{-1}$) consists of the thermal resistance of the nanowire (R_n) and the total contact thermal resistance between the nanowire and the two membranes (R_c), i.e.,

$$R_m = R_n + R_c \qquad (6)$$

To reduce R_c, we used focused electron beam deposition or focused ion beam deposition to deposit a Pt layer locally on the contacts from precursor gases in a dual beam focused ion beam (FIB) tool. The deposited Pt layer is shown in Figure 4. It was found that the Pt layer deposited by focused electron beam reduces the obtained R_m for about 10% for a 152-nm-diameter carbon nanofiber sample.[48] To minimize the spreading of Pt and to prevent the conversion of residual precursor gas species absorbed on the sample surface into a conducting layer, we avoided imaging the sample using either the electron or ion beam right after the Pt deposition. Additionally, we avoided imaging the suspended segment of the nanowire with either ion beam or high-magnification SEM in order to prevent sample damage or contamination.

Electrical Conductance Measurement. There is often a native oxide layer on a nanowire, resulting in large electrical contact resistance between the nanowire and the Pt electrodes. This large contact resistance can be reduced by depositing a Pt line locally on top of the contact between the nanowire and the Pt electrode, using the focused electron beam or a focused ion beam deposition method. The two as-deposited Pt lines allowed for the simultaneous measurement of S and κ of the nanowire. After the measurements of S and κ, two additional Pt lines can be deposited to connect the nanowire with the two Pt serpentine lines on the two membranes, as shown in Figure 2, so as to measure the four-probe electrical resistance (R_{4p}) of the nanowire. The two additional Pt lines were used as the outer electrodes for current source and drain, and the two middle Pt electrodes served as the voltage probes in the R_{4p} measurement.
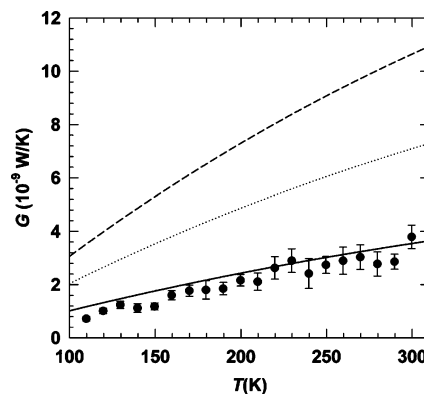

Figure 5. Thermal conductance (G) of the SWCNT as a function of the temperature (T). Filled circles are the measurement results. The solid, dotted, and dashed lines are the ballistic thermal conductance of a 1-nm-, 2-nm, and 3-nm -diameter SWCNT, respectively, calculated by Mingo and Broido.[50] Reproduced with permission from ref 49. Copyright 2005 American Chemical Society.

Seebeck Coefficient Measurement. The temperature difference of the two membranes yields a TE voltage that can be measured using the two Pt electrodes contacting the nanostructure, i.e., $V_{TE} = (S_s - S_{Pt})(\Delta T_h - \Delta T_s)$. The Seebeck coefficient (S_{Pt}) of the Pt electrode is small[25] and can be ignored. By measuring ΔT_h, ΔT_s, and V_{TE}, the Seebeck coefficient (S_s) of the sample can be obtained.

III. Thermal Conductance of SWCNTs

We have used the microdevice to measure the thermal conductance (G) of an isolated suspended SWCNT shown in Figure 3 in the temperature range between 110 and 300 K.[49] SWCNTs are visible in SEM due to electron charging. High-magnification SEM measurement indicates that the diameter (d) of the SWCNT should be less than 5 nm. However, an accurate diameter measurement with the SEM was not feasible due to its resolution of about 3 nm. The substrate of the suspended micro-device was not completely etched through so that transmission electron microscopy (TEM) measurement of the SWCNT diameter was not feasible. Instead, we have conducted atomic force microscopy (AFM) measurement of the diameter of a large number of SWCNTs grown using the same method on silicon substrates. The diameter was in the range of 1−2 nm for most of the SWCNTs, while occasionally a diameter of 2−3 nm was observed.

As shown in Figure 5, the measured thermal conductance of the SWCNT increases with temperature from 0.7×10^{-9} W/K at 110 K to 3.8×10^{-9} W/K at 300 K. The measurement result was very close to the calculated ballistic thermal conductance of a 1-nm-diameter SWCNT and was about 50% and 30% of the ballistic thermal conductance of a 2-nm and 3-nm diameter SWCNT, respectively. The diameter of the SWCNT should not be smaller than 1 nm because the measurement result was larger than the calculated ballistic thermal conductance of a SWCNT with $d < 1$ nm. The ballistic thermal conductance is the maximum possible value calculated by Mingo and Brodio[50] for the case that phonon transport is ballistic in the SWCNT and phonons from the SWCNT enter the two contacts without suffering reflection. In the calculation, the temperature of the phonon flow entering the SWCNT from each contact equals that of the contact along the entire length of the SWCNT, as illustrated in Figure 6. Due to the absence of scattering, the two opposite phonon flows are at two different temperatures and not at equilibrium with each other. The obtained ballistic thermal conductance is not infinite because the phonon flow is
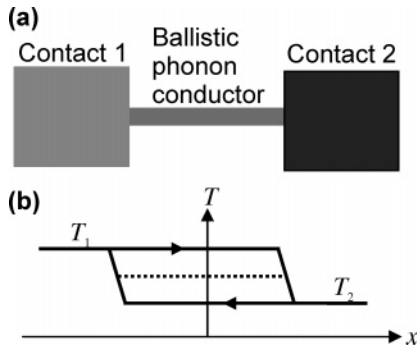
Figure 6. (a) Schematic diagram of a 1D ballistic phonon conductor connected to two side contacts at different temperatures, i.e., T_1 and T_2. (b) The temperature distribution of the two opposite phonon flows inside the ballistic phonon conductor. The dotted line is the average temperature of the two phonon flows. Reproduced with permission from ref 49. Copyright 2005 American Chemical Society.

Figure 7. Thermal conductivity (κ) of the SWCNT if the diameter was 1 nm (filled circles), 2 nm (open circles), and 3 nm (filled triangles). The line is the measurement result of an individual MWCNT from Kim et al. (Phys. Rev. Lett. **2001**, 87, 215502). Reproduced with permission from ref 49. Copyright 2005 American Chemical Society.

TABLE 1: Diameter (d) and the Measured Properties of the Nanowires

sample	1(2 wires)	2	3	4
batch	1	1	1	2
d (nm)	100 each	57.5	43.5	81
properties	S, G	σ	σ	S, σ, κ, ZT

scattered after it exits the SWCNT and enters the opposite contact in order for the phonon flow to adopt the different temperature of the contact. Hence, the ballistic thermal conductance is essentially the maximum contact thermal conductance between the SWCNT and the two thermal reservoirs.

The calculated ballistic thermal conductance consists of only the contribution from phonons, i.e., G_p. It has been calculated that the electron contribution (G_e) is negligible compared to G_p at moderate temperatures.[51] In the temperature range between 110 and 300 K, the measured thermal conductance of the SWCNT consists of mainly the phonon contribution.

Mingo and Brodio[50] noted that the measured G of an individual MWCNT[52] was close to 40% of the ballistic thermal conductance of graphite for $T < 300$ K. Here, the measured G of the SWCNT is also proportional to the ballistic thermal conductance for SWCNTs in the temperature range between 100 K and 300 K. Phonons can be reflected when entering the two contacts from the CNT, lowering the thermal conductance of the CNT to a fraction of the ballistic thermal conductance. Additionally, local defects in the suspended CNT can reduce the phonon transmission coefficient, lowering G to a fraction of the ballistic thermal conductance. The G reduction due to these two effects is approximately temperature-independent to the first order, and the resulting G vs T curve is proportional to the ballistic thermal conductance. On the other hand, the phonon–phonon Umklapp scattering process can reduce G from the ballistic thermal conductance, and a larger reduction is expected at higher temperatures, making the G vs T curve deviate from the trend of the ballistic thermal conductance. Since the measured G vs T curve is proportional to the ballistic thermal conductance at $T < 300$ K for both the SWCNT and the MWCNT, we conclude that Umklapp process was insignificant in both samples at $T < 300$ K.

The thermal conductivity of the SWCNT was calculated for the case that the diameter was 1, 2, and 3 nm, according to $\kappa = GL/A$, where L is the length of the suspended segment of the SWCNT between the two membranes and A is the cross-sectional area, which is not a well-defined quantity for a SWCNT. We followed ref 50 to calculate $A = \pi d\delta$, where $\delta = 0.335$ nm is the layer separation in graphite. The obtained κ in Figure 7 is on the same order of magnitude as the measurement results of an individual MWCNT,[52] which is also shown in the figure. More accurate measurement of the thermal conductivity can be obtained if a through-hole is etched in the substrate of the microdevice to allow for accurate TEM measurement of the diameter of the SWCNT.
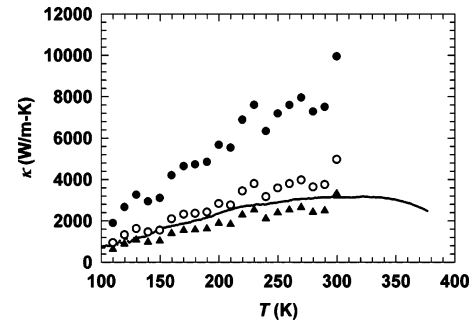
IV. Thermoelectric Properties of Bi_xTe_{1-x} Nanowires

We have measured the thermoelectric properties of two batches of bismuth telluride (Bi_xTe_{1-x}) nanowires with different atomic ratio or x.[53,54] The Bi_xTe_{1-x} nanowires were deposited in the nanopores of anodized alumina membranes (AAMs) with the use of an electrochemical deposition method.[55] The growth direction of the nanowire was $\langle 11\bar{2}0\rangle$, perpendicular to the c-axis. During the deposition, the Bi to Te atomic ratio in the electrolytes was 2 to 3 for the first batch and 1 to 1 for the second batch. High-resolution transmission electron microscopy (HRTEM) measurements of the nanowires revealed that these nanowires were single crystalline, and the native surface oxidation layer was about 2–10 nm thick. The chemical composition of one nanowire from the first batch and four nanowires from the second batch were obtained with the use of an energy dispersive spectrometer (EDS) of the HRTEM. The Bi-to-Te ratio of the nanowire from the first batch was 46% to 54%. The average EDS-obtained atomic fraction of the four nanowires from the second batch is 54% of Bi and 46% of Te with a standard deviation of 4.2%.

We have measured different properties of the four samples listed in Table 1 from the two different batches. Among these samples, sample 1 consists of two nanowires whereas all other samples consist of only one nanowire.

For sample 1 from the first batch, the obtained S in Figure 8 was positive, indicating that the nanowire was p-type. For this
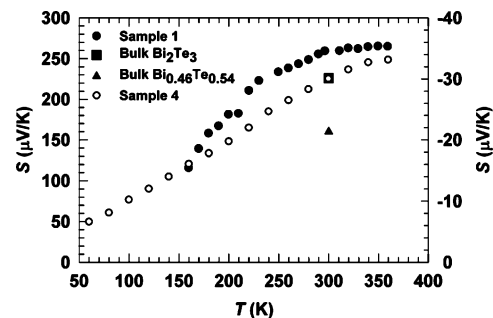

Figure 8. Seebeck coefficient as a function of temperature for sample 1, sample 4, bulk Bi_2Te_3, and bulk $Bi_{0.46}Te_{0.54}$. The left Y axis is for filled symbols and the right Y axis is for unfilled symbols. Reproduced with permission from ref 53. Copyright 2005 American Institute of Physics.
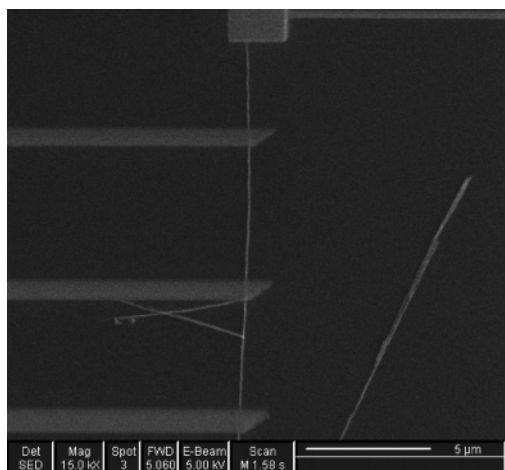
Feature Article

J. Phys. Chem. B, Vol. 109, No. 47, 2005 **22107**

Figure 9. SEM image of a bismuth telluride nanowire deposited on a substrate with four Pt contacts patterned on top of the nanowire.
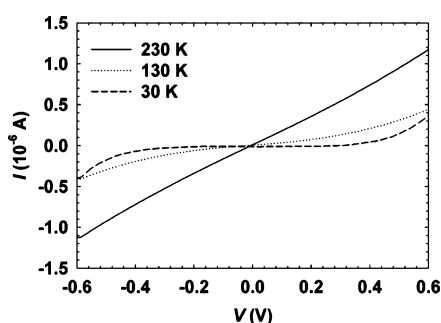

Figure 10. Measured two-probe $I-V$ curves for Bi_xTe_{1-x} nanowire sample 1 at temperature 230, 130, and 30 K.

Figure 11. Two-probe (R_{2p}) and four-probe (R_{4p}) electrical resistances of Bi_xTe_{1-x} nanowire sample 1, 2, and 3 as a function of temperature.

Figure 12. Electrical conductivity (σ) of the nanowires (filled symbols) and bulk crystals (open symbols) as a function of temperature. Reproduced with permission from ref 53. Copyright 2005 American Insitute of Physics.

sample, the value of 260 μV/K at $T = 300$ K was 60% higher than that for bulk $Bi_{0.46}Te_{0.54}$ crystal,[25] which has an atomic ratio similar to that of the first batch, and 15% higher than that of Bi_2Te_3, which was found to have the largest S for p-type Bi_xTe_{1-x} bulk crystals.[25] For sample 4 from the second batch, S was negative, suggesting electron-like majority carriers. As a comparison, bulk Bi_xTe_{1-x} crystals are p-type for $x > 0.37$, n-type for $x < 0.37$, and bulk $Bi_{0.485}Te_{0.505}$ is highly p-doped.[25,56] A different crystal phase might have developed for the second batch of nanowires with $x \approx 0.54$, leading to the negative S.

The R_{4p} of three samples has been measured. For samples 2 and 3, the nanowire was deposited on an oxidized silicon wafer, and four Pt electrodes were patterned on the nanowire by FIB deposition, as shown in Figure 9. There was no electrical leakage between two Pt electrodes after a 100 nm wide cut was made by FIB on the nanowire between the two electrodes, suggesting Pt spreading was minimized during the Pt deposition. For sample 4, four Pt electrodes were patterned on the nanowire segments laid on the suspended microdevice using focused ion beam (FIB) deposition, similar to Figure 2.

The two-probe current–voltage ($I-V$) curves for sample 1 were rather linear in the temperature range between 240 and 360 K, but show nonlinear behavior of a Schottky contact at $T < 230$ K, as shown in Figure 10. Linear two-probe $I-V$ curves were observed for sample 2 at $T > 4$ K and for sample 3 at $T > 120$ K. On the other hand, all the four-probe $I-V$ curves were linear, suggesting that the Schottky contact resistance was eliminated in the four-probe measurement. The two-probe resistance (R_{2p}) of sample 1 was calculated from the linear $I-V$ curves and is shown in Figure 11 together with the R_{2p} and R_{4p} of sample 2 and sample 3 from the same batch.
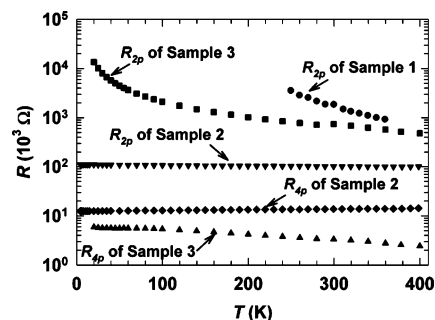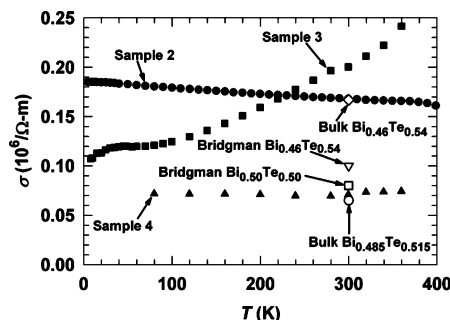
The σ values calculated from R_{4p} are shown in Figure 12 together with the reported room-temperature σ for bulk $Bi_{0.46}$-$Te_{0.54}$ and $Bi_{0.485}Te_{0.505}$ crystals. The room-temperature σ of sample 2 and sample 3, both from the first batch, were within 10% difference from those reported for bulk $Bi_{0.46}Te_{0.54}$ and the Bridgman-type $Bi_{0.46}Te_{0.54}$ single crystals.[56] While it has been found that the bulk σ decreases approximately linearly with increasing temperature as a result of increased electron–phonon scattering,[56] the σ of the nanowires shows a very weak temperature dependence. For sample 2, the decrease of σ with increasing temperature was somewhat similar to but at a much smaller slope than the bulk behavior. While the smaller slope can be attributed to a surface-scattering dominated electron mean free path that is insensitive to the temperature, the room-temperature σ was not reduced by enhanced surface scattering. The behavior of sample 3 is somewhat similar to that of a semiconductor, for which an increase of the carrier concentration can lead to an increased σ with increased temperature. Additionally, the presence of local defects or conduction barriers in the nanowire can lead to the increased σ with temperature.

The σ of sample 4 from the second batch was almost independent of temperature. The room-temperature value was within 10% difference from those for bulk $Bi_{0.485}Te_{0.515}$ and Bridgman-type $Bi_{0.50}Te_{0.50}$ single crystals.[56]

The κ of the three samples from the first batch were not obtained, and only the G of sample 1 was obtained. The κ of sample 4 from the second batch has been measured, and the measurement results are shown in Figure 13 together with the obtained G of sample 1 from the first batch.

For bulk Bi_2Te_3, the thermal conductivity peaks at a temperature below 75 K and decreases from 75 K to a minimum at about 270 K due to the Umklapp phonon–phonon scattering.[57] Additionally, the electron and phonon contributions to the thermal conductivity of bulk Bi_2Te_3 are approximately 46% and 54%, respectively, at 300 K.[25]
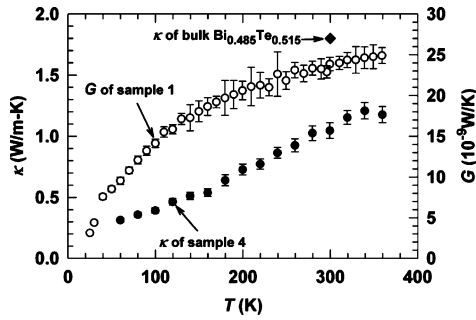
Figure 13. Thermal conductivity (κ, filled symbols) or thermal conductance (G, open symbols) as a function of temperature. Reproduced with permission from ref 53. Copyright 2005 American Institute of Physics.
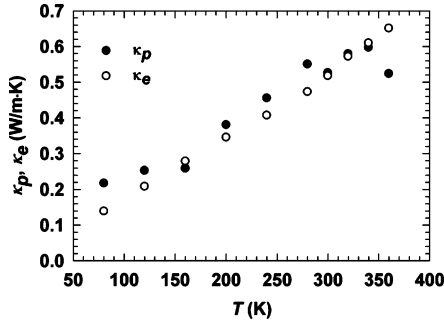

Figure 14. Calculated κ_p and κ_e of Bi_xTe_{1-x} nanowire sample 4.

For sample 1, G increased with T and approached a maximum value at $T > 350$ K. The shift of the maximum G and thus κ to high T is an indication that phonon-boundary scattering dominates phonon−phonon Umklapp scattering for $T < 300$ K. For sample 4, κ increased as T and reached a maximum value at $T \approx 340$ K. Similar to sample 1, phonon-boundary scattering was the dominant scattering process at $T < 300$ K.

The room-temperature κ value of sample 4 was about 40% lower than those reported in ref 56 of bulk $Bi_{0.485}Te_{0.515}$ crystals, as shown in Figure 13. The κ_p and κ_e of this sample have been calculated according to the Wiedemann−Franz law with the Lorenz number $L = 2.44 \times 10^{-8}$ W-Ω/K^2. The ratio between κ_p and κ_e was 1.02 at room temperature, as shown in Figure 14. As a comparison, this ratio is 2.39 for bulk $Bi_{0.485}Te_{0.515}$ crystal[25] and 1.17 for bulk Bi_2Te_3 cystal[25,56] if the same L value is used. The obtained room temperature κ_p of sample 4 was 60% lower than that of bulk $Bi_{0.485}Te_{0.515}$. On the other hand, the room-temperature σ and κ_e of the nanowire was only 5.6% lower than the value for the bulk $Bi_{0.485}Te_{0.515}$. The large difference in the percentage reductions in κ_p and σ can have two possible origins. First, the de Broglie wavelength (λ_e) of electrons in these semiconductor nanowires is about 10 nm; while the phonon wavelength (λ_{ph}) is of the order of 1 nm. For a surface roughness (r) on the order of 1 nm, the scattering cross section is proportional to (r/λ),[4] where λ is the wavelength and is much smaller for electrons than for phonons. Thus, one expects that the surface roughness may reduce κ_p to a much larger extent than the reduction in σ. Because the chemical composition of the nanowire is different from that of the bulk crystal used for comparison, however, it is possible that an increase of x from $x = 0.485$ for the bulk crystal to $x = 0.54$ for the nanowire possibly leads to an increase in σ and a reduction in κ_p, although σ was found to be reduced more than κ_p when x was increased from 0.4 to 0.485 for the bulk crystals. In fact, for this nanowire from the second batch, the ZT shown in Figure 15 was rather low due to the low S value at this chemical composition.
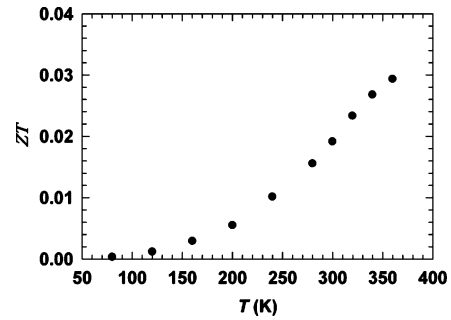

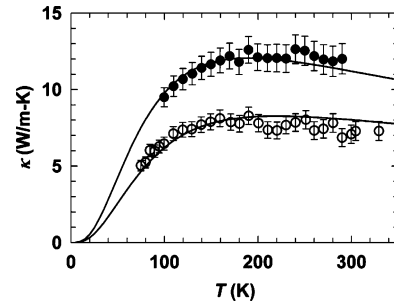**Figure 15.** Thermoelectric figure of merit (ZT) of Bi_xTe_{1-x} nanowire sample 4.

Figure 16. Thermal conductivity of a 64-nm-thick (solid circles) and a 53-nm-thick (open circles) SnO_2 nanobelt as a function of temperature. Also shown are calculation results (lines) with the bulk parameters for phonon−phonon Umklapp scattering and phonon-impurity scattering and different FL values of 64 nm for the upper line and 39 nm for the lower line. Reproduced with permission from ref 58. Copyright 2004 American Institute of Physics.

For Bi_xTe_{1-x} nanowires from the first batch with $x \approx 0.46$, we found that the S was 15%−60% higher than and σ was within 10% difference from the corresponding bulk values. We also observed signatures of increased phonon-boundary scattering that should reduce the lattice thermal conductivity. These evidences suggest that high ZT can potentially be obtained in Bi_xTe_{1-x} nanowires with an optimized atomic ratio.

V. Thermal Conductivity of Metal Oxide Nanowires

We have employed the microdevice to measure the thermal conductivity of 53-nm-thick, 204-nm-wide, and 64-nm-thick, 108-nm-wide SnO_2 nanobelts in the temperature range of 80−350 K.[58] As shown in Figure 16, the obtained κ values were found to be substantially lower than the bulk values.[59]

To understand the origins of the reduced κ, we have compared the measurement results with a full dispersion transmission function calculation.[60] In the calculation, the phonon dispersion relation was obtained for the rutile structure. Matthiessen's rule was used to obtain the frequency-dependent relaxation time of phonons as $\tau^{-1} = \tau_U^{-1} + \tau_b^{-1} + \tau_i^{-1}$.[61,62] Here, τ_U^{-1}, τ_b^{-1}, and τ_i^{-1} are the Umklapp, boundary, and impurity scattering rates, respectively. A phenomenological expression for the Umklapp scattering rate has been used: $\tau_U^{-1} = Be^{-b/T}\omega^2 T$, where B and b are two fitting parameters and ω is the phonon frequency. The boundary and impurity scattering rates can be written as $\tau_b^{-1} = v/FL$ and $\tau_i^{-1} = A\omega^4$. Here, v is the phonon group velocity, L is the thickness for the nanobelt, F is a parameter representing specularity of phonon reflection at the boundaries, the FL product is referred as the effective thickness of the sample, and A is a parameter arising from Rayleigh scattering of phonons by atomic scale impurities.

After obtaining the fitting parameters from the measurement data obtained for bulk crystals, the thermal conductivity of

Feature Article

J. Phys. Chem. B, Vol. 109, No. 47, 2005 **22109**

nanowires was calculated for different effective thickness *FL*, with other parameters kept as the same as the bulk values. The solid lines of Figure 16 are two sets of calculated κ in the (101) direction as a function of temperature. One can see that the measurement data of the 64-nm-thick and 53-nm-thick SnO_2 nanobelt agree rather well with the calculation results with *FL* = 64 and 39 nm, respectively. This suggests that an increased phonon-boundary rate alone can well account for the significantly suppressed κ of the nanobelts. Increased phonon-boundary scattering alone can also account for another measurement result of the suppressed κ of silicon nanowires,[63,64] except for a 22-nm-diameter Si nanowire, the smallest one of the samples, where other phonon confinement effects may have also play a role.

VI. Integration of Nanowires with Microdevices for Sensor Systems

In addition to providing an ideal system for investigating phonon transport in dimension-confined systems, the single-crystal metal oxide nanobelts are very attractive for sensor applications. Metal oxide sensors are commonly used for the detection of inflammable and toxic gas species. The sensing mechanism is based on resistivity change upon surface reduction−oxidation (redox) reactions with gas species.[65] Because only the surface layer is affected by the reaction, the sensitivity of a metal oxide sensor increases for decreasing thickness, motivating the development of thin film metal oxide sensors. However, one common problem with polycrystalline thin film metal oxide sensors is grain boundary poisoning that limits the repeatability and long-term stability.[66,67] Because the nanobelts are as thin as 10 nm, which approaches the electrostatic screening length, almost the entire thickness is affected by redox reactions with gas species, leading to high sensitivity.[68]

Metal oxide sensors require a high operating temperature to enhance redox reactions so as to achieve the optimum sensitivity. This requirement has motivated us to integrate nanobelts with thermally isolated suspended micro-heater devices that can reduce the power consumption so that battery-operated miniaturized sensor arrays can be obtained. More importantly, a major challenge for the development of sensor technologies based on nanobelts or other "bottom-up" synthesized nanostructures is the large-scale manufacturing of well-organized nanostructure sensor arrays. To address this challenge, we have investigated the assembly of nanobelts with the "top-down" fabricated MEMS device that was developed for thermal characterization of nanowires. We found that positive DEP can be used for the assembly of nanobelts with the MEMS device at a high yield.

The two membranes of the microdevice were supported by long, low-thermal conductivity silicon nitride (SiN_x) beams and were thermally isolated from the substrate. The temperature of the membrane can be increased and monitored with the use of the PRT serpentine patterned on the membrane. With only 3.8 mW power consumption in the Pt RT, the membrane temperature can be raised to 500 °C.

We have tested the device shown in Figure 17 that had one nanobelt trapped between the two Pt electrodes. We used a FIB method to deposit a thin Pt coating on the nanobelt so as to improve the electrical contact. The sensor was mounted in a small flow-through chamber and tested with NO_2 and dimethyl methyl phosphonate (DMMP) gases diluted in air.

Figure 18 shows the response of the nanobelt sensor to 0.2−10 ppm NO_2 gas balanced in air while the nanobelt was heated to 200 °C by the microheater. Current change in the nanobelt was clearly observed when the NO_2 concentration was as low as 200 ppb. The sensitivity can potentially be improved with
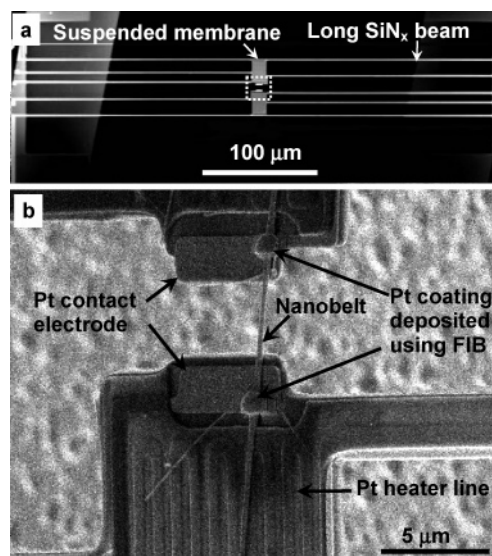

Figure 17. (a) SEM image of the microheater device. (b) An enlarged image showing the region inside the white dashed rectangle in a. Reproduced with permission from ref 42. Copyright 2005 American Institute of Physics.
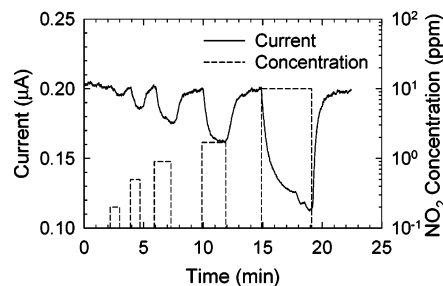

Figure 18. Response of the as-assembled nanobelt-MEMS sensor to 0.2, 0.5, 0.9, 1.7, and 10 ppm NO_2 balanced with air when the nanobelt temperature was 200 °C. The voltage applied to the nanobelt was 2 V. Reproduced with permission from ref 42. Copyright 2005 American Institute of Physics.

the optimization of the heater temperature and with the doping of the nanobelt with catalytic additives to increase its electrical conductivity and enhance redox processes.[69]

Further, it was found that the current through the nanobelt recovered fully quickly after the NO_2 gas was shut off and the flow-though chamber was purged with room air. The recovery was much faster than that of the bunch of nanobelts tested in an earlier work.[68] It took less than three minutes, which could be the time required for completely purging NO_2 out of the flow-through chamber, for the single nanobelt sensor to be refreshed. On the other hand, the bunch of nanobelts in the earlier work was not completely refreshed 40 min after the NO_2 gas was shut off.

The faster recovery observed in the nanobelt was attributed to the absence of grain boundaries or interfaces along the isolated nanobelt of a single-crystal structure. In fact, we found that the Pt coating deposited on the nanobelt by the FIB method was critical for eliminating the sensor poisoning effect. Without this contact treatment, it was observed that even a sensor consisting of just a single nanobelt could be poisoned, i.e., the current could not recover fully after the NO_2 gas was shut off. With the contact treatment, on the other hand, this poisoning effect was completely eliminated, suggesting that the single-crystal nanobelt itself was not poisoned but a poor contact between the nanobelt and the Pt electrode could still be poisoned. This finding suggests that the slow recovery observed in the
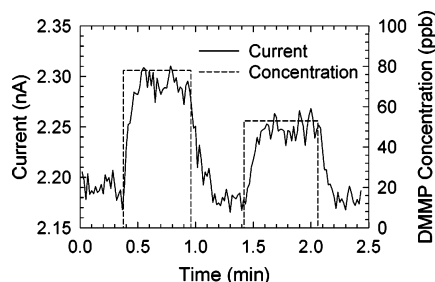
Figure 19. Response of the as-assembled nanobelt sensor to 78 and 53 ppb DMMP balanced with air when the nanobelt temperature was 500 °C. The voltage applied to the nanobelt was 1.5 V. Reproduced with permission from ref 42. Copyright 2005 American Institute of Physics.

bunch of nanobelts tested in the earlier work[68] was due to poisoning either at the poor contacts between the nanobelts and the electrodes or at the interfaces between connecting nanobelts in the bunch of nanobelts. The elimination of such poisoning is essential for obtaining high sensor stability and repeatability.

We have also tested another as-assembled nanobelt sensor consisting of a single nanobelt with diluted DMMP gas obtained from a permeation tube containing a liquid phase of DMMP. Figure 19 shows the sensor response to DMMP gas balanced with air when the device was Joule-heated to 500 °C. The current through the nanobelt increased for about 5% and 3%, respectively, in respond to the 78 and 53 ppb DMMP diluted in air. This sensitivity can potentially be enhanced to sub-ppb levels by doping the nanobelt with CaO, a catalytic additive for increasing the sensitivity of metal oxide sensors for DMMP detection.[69] Most importantly, in contrast with thin film metal oxide sensors for DMMP detection,[70] the as-assembled nanobelt sensor did not show any poisoning effect upon exposure to DMMP and the current recovered quickly as DMMP was shut off.

VII. Concluding Remarks and Future Directions

These experiments employing MEMS devices show that CNTs have super-high thermal conductivity with potential applications as heat spreaders in electronic packaging applications, that the thermal conductivity of semiconductor and metal oxide nanowires are suppressed due to phonon-boundary scattering, and that high thermoelectric figure of merit can potentially be obtained in bismuth telluride and other semiconductor nanowires. It was found in our measurements that the thermal and thermoelectric properties of individual nanowires and nanotubes are largely influenced by the crystal structure including crystalline quality, chemical composition, and surface roughness. In the experiments reviewed in this article, the physical properties and crystal structure were not obtained on the same nanostructures and the correlation between the crystal structure and thermoelectric properties could not be established. We have a current effort to improve the MEMS device in order to characterize the structure and properties of the same individual nanostructure. In the new design, a through hole is etched in the substrate of the suspended device to allow for transmission electron microscopy (TEM) and energy dispersion spectroscopy (EDS) measurements of the nanostructure. The obtained crystalline quality, surface roughness, and chemical composition can be correlated with the obtained thermal and thermoelectric properties. Additionally, micro Raman spectroscopy[71] or Raleigh scattering measurements[72] can also be employed to characterize the nanostructure assembled on the microdevice. These measurements will potentially provide a comprehensive set of structure and property data on the same nanostructure, which will be invaluable for improving our understanding of the effects of nanostructures on charge and phonon transports.

Furthermore, a method has been developed elsewhere for measuring the mechanical properties such as elastic modulus of individual CNT.[73] This mechanical measurement method can potentially be integrated with the microdevice that we developed for thermal measurements. The integration can be obtained with the addition of a microactuator to control the lateral movement of one of the two SiN_x membranes, so that the thermal property can be measured as a function of stress in the nanowire. The obtained results can be highly useful, because the thermal and thermoelectric properties depend on stress in the materials. In fact, high *ZT* has been observed in bulk crystals under a compressive stress,[74] and the charge transport property in CNTs has been known to be sensitive to bending.[75]

In the direction of the large-scale integration of nanowires for sensor systems, the recent development of controlled nanowire assembly and growth methods can enable wafer-scale fabrication of micromachined sensor arrays containing multiple layers of different surface-functionalized nanowire sensor elements with different catalytic additives for ultrasensitive and stable detection of chemical species and biomolecules. It has been reported that the Langmuir–Blodgett (L–B) method can allow for the large-scale assembly of aligned nanowire monolayers.[76,77] Similar to a metal oxide thin film deposited using a physical vapor deposition (PVD) method, the L–B nanowire monolayer can be patterned using conventional photolithography and etching. Multiple metal oxide nanowire films can be sequentially deposited using the room-temperature L–B method and patterned using photolithography. The room-temperature L–B deposition eliminates mass diffusion between adjacent layers of metal oxides, a major problem in the fabrication of thin film metal oxide sensor arrays using high-temperature PVD of multiple metal oxide films. This method will likely allow for the fabrication of selective gas sensor arrays consisting of functionalized metal oxide nanobelts integrated with a MEMS platform that consists of a microchromatography column and preconcentrator for gas separation and preconcentration. Alternatively, the selectivity can also be obtained with the use of a pattern recognition approach, where an array of sensors made of different metal oxides with different catalytic additives generates a distinct response pattern for a gas species or mixture.

References and Notes

(1) Dresselhaus, M. S.; Dresselhaus, G.; Eklund, P. C. *Science of Fullerenes and Carbon Nanotubes*; Academic Press: New York, 1996.

(2) Lieber, C. M. *MRS Bull.* **2003**, *28*, 486.

(3) Tans, S. J.; Verschueren, A. R. M.; Dekker, C. *Nature* **1998**, *393*, 49.

(4) Dekker, C. *Phys. Today* **1999**, May 22.

(5) Postma, H. W. Ch.; Teepen, T.; Yao, Z.; Grifoni, M.; Dekker, C. *Science* **2001**, *293*, 5527.

(6) McEuen, P. L.; Fuhrer, M. S.; Park, H. *IEEE Trans. Nanotechnol.* **2002**, *1*, 78.

(7) Bachtold, A.; Hadley, P.; Nakanishi, T.; Dekker: C. *Science* **2001**, *294*, 1317.

Feature Article

J. Phys. Chem. B, Vol. 109, No. 47, 2005 **22111**

(8) Derycke, V.; Martel, R.; Appenzeller, J.; Avouris, Ph. *Nano Lett.* **2001**, *1*, 453.

(9) Huang, M. H.; Mao, S.; Feick, H.; Yan, H.; Wu, Y.; Kind, H.; Weber, E.; Russo, R.; Yang, P. *Science* **2001**, *292*, 5523.

(10) Kong, J.; Franklin, N. R.; Zhou, C.; Chapline, M. G.; Peng, S.; Cho, K.; Dai, H. *Science* **2000**, *287*, 622.

(11) Cui, Y.; Wei, Q. Q.; Park, H. K.; Lieber, C. M. *Science* **2001**, *293*, 1289.

(12) de Heer, W. A.; Châtelain, A.; Ugarte, D. *Science* **1995**, *270*, 1179.

(13) Wang, Q. H.; Setlur, A. A.; Lauerhaas, J. M.; Dai, J. Y.; Seelig, E. W.; Chang R. P. H. *Appl. Phys. Lett.* **1998**, *72*, 2912.

(14) Choi, W. B.; Chung, D. S.; Kang, J. H.; Kim, H. Y.; Jin, Y. W.; Han, I. T.; Lee, Y. H.; Jung, J. E.; Lee, N. S.; Park, G. S.; Kim J. M. *Appl. Phys. Lett.* **1999**, *75*, 3129.

(15) Dresselhaus, M. S.; Dresselhaus, G.; Sun, X.; Zhang, Z.; Cronin, S. B.; Koga, T.; Ying, J. Y.; Chen G. *Microscale Thermophys. Eng.* **1999**, *3*, 89.

(16) Volz, S. G.; Chen, G. *Appl. Phys. Lett.* **1999**, *75*, 2056.

(17) Khitun, A.; Balandin, A.; Wang, K. L. *Superlattices Microstruct.* **1999**, *26*, 181.

(18) Schelling, P.; Shi, L.; Goodson, K. E. *Mater. Today* **2005**, *8*, 30.

(19) Goodson, K. E. *ASME J. Heat Transfer* **1996**, *118*, 279.

(20) Berber, S.; Kwon, Y.-K.; Tomanek, D. *Phys. Rev. Lett.* **2000**, *84*, 4613.

(21) Osman, M. A.; Srivastava, D. *Nanotechnology* **2001**, *12*, 21.

(22) Li, J.; Ye, Q.; Cassell, A.; Ng H. T.; Stevens, R.; Han, J.; Meyyappan, M. *Appl. Phys. Lett.* **2003**, *82*, 2491.

(23) Nihei, M.; Kawabata, A.; Kondo, D.; Horibe, M.; Sato, S.; Awano, Y. *Jpn. J. Appl. Phys.* **2005**, *44*, 1626.

(24) Nolas, G. S.; Sharp, J.; Goldsmid, H. J. *Thermoelectrics: Basic Principles and New Materials Development*; Springer-Verlag: Berlin, Heidelberg, 2001.

(25) D. M. Rowe *CRC Handbook of Thermoelectrics*; CRC Press: Boca Raton, FL 1995.

(26) Hicks, L. D.; Dresselhaus, M. S. *Phys. Rev. B* **1993**, *47*, 16631.

(27) Hicks, L. D.; Dresselhaus, M. S. *Phys. Rev. B* **1993**, *47*, 12727.

(28) Chen, G.; Shakouri, A. *ASME J. Heat Transfer* **2002**, *124*, 242.

(29) Venkatasubramanian, R.; Siivola, E.; Colpitts, T.; O'Quinn, B. *Nature* **2001**, *413*, 597.

(30) Harman, T. C.; Taylor, P. J.; Walsh, M. P.; LaForge, B. E. *Science* **2002**, *297*, 2229.

(31) Hsu, K. F.; Loo, S.; Guo, F.; Chen, W.; Dyck, J. S.; Uher, C.; Hogan, T.; Polychroniadis, E. K.; Kanatzidis, M. G. *Science* **2004**, *303*, 818.

(32) Lin, Y.-M.; Sun, X.; Dresselhaus, M. S. *Phys. Rev. B* **2000**, *62*, 4610.

(33) Mingo, N. *Appl. Phys. Lett.* **2004**, *84*, 2652.

(34) Hone, J.; Whitney, M.; Piskoti, C.; Zettl, A. *Phys. Rev. B* **1999**, *59*, R2514.

(35) Hone, J.; Llaguno, M. C.; Nemes, N. M.; Johnson, A. T.; Fischer, J. E.; Walters, D. A.; Casavant, M. J.; Schmidt, J.; Smalley, R. E. *Appl. Phys. Lett.* **2000**, *77*, 666.

(36) Shi, L.; Li, D.; Yu, C.; Jang, W.; Yao, Z.; Kim, P.; Majumdar, A. *ASME J. Heat Transfer* **2003**, *125*, 881.

(37) Lin, Y.; Cronin, S. B.; Ying, J. Y.; Dresselhaus, M. S. *Appl. Phys. Lett.* **2000**, *76*, 3944.

(38) Lin, Y.; Cronin, S. B.; Rabin, O.; Ying, J. Y.; Dresselhaus, M. S. *Appl. Phys. Lett.* **2001**, *79*, 677.

(39) Yi, W.; Lu, L.; Zhang D. L.; Pan, Z. W.; Xie, S. S. *Phys. Rev. B* **1999**, *59*, R9015.

(40) Choi T. Y.; Poulikakos, D.; Tharian, J.; Sennhauser, U. *Appl. Phys. Lett.* **2005**, *87*, 013108.

(41) Datta, S. *Electronic Transport in Mesoscopic Systems*; Cambridge University Press: Cambridge, UK 1999.

(42) Yu, C.; Hao, Q.; Saha, S.; Shi, L.; Kong, X.; Wang, Z. L. *Appl. Phys. Lett.* **2005**, *86*, 063101.

(43) Jones, T. B. *Electromechanics of Particles*; Cambridge University Press: New York, 1995.

(44) Chen, X. Q.; Saito, T.; Yamada, H.; Matsushige, K. *Appl. Phys. Lett.* **2001**, *78*, 3714.

(45) Smith, P. A.; Nordquist, C. D.; Jackson, T. N.; Mayera, T. S.; Martin, B. R.; Mbindyo, J.; Mallouk, T. E. *Appl. Phys. Lett.* **2000**, *77*, 1399.

(46) Duan, X.; Huang, Y.; Cui, Y.; Wang, J.; Lieber, C. M. *Nature* **2001**, *409*, 66.

(47) Kong, J.; Soh, H.; Cassell, A.; Quate, C. F.; Dai, H. *Nature* **1998**, *395*, 878.

(48) Yu, C.; Shi, L.; Saha, S.; Zhou J.; Cassell, A. M.; Cruden, B. A.; Ngo, Q.; Li, J. *ASME J. Heat Transfer*, March 2006.

(49) Yu, C.; Shi, L.; Yao, Z.; Li, D.; Majumdar A. *Nano Lett.* **2005**, *5*, 1842.

(50) Mingo, N.; Broido, D. A. *Phys. Rev. Lett.* **2005**, *95*, 096105.

(51) Yamamoto, T.; Watanabe, S.; Watanabe, K. *Phys. Rev. Lett.* **2004**, *92*, 075502.

(52) Kim, P.; Shi, L.; Majumdar, A.; McEuen, P. L. *Phys. Rev. Lett.* **2001**, *87*, 215502.

(53) Zhou, J.; Jin, C. Q.; Seol, J. H.; Li, X. G.; Shi, L. *Appl. Phys. Lett.* **2005**, *87*, 133109.

(54) Zhou, J.; Jin, C. Q.; Seol, J. H.; Li, X. G.; Shi, L. *Proc. 24th Int. Thermoelectrics Conf.* 2005, in print.

(55) Jin, C.; Xiang, X.; Jia, C.; Liu, W.; Cai, W.; Yao, L.; Li, X. *J. Phys. Chem. B* **2004**, *108*, 1844.

(56) Fleurial, J. P.; Gailliard, L.; Triboulet, R.; Scherrer, H.; Scherrer, S. *J. Phys. Chem. Solids* **1988**, *49*, 1237.

(57) Satterthwaite, C. B.; Ure, R. W., Jr. *Phys. Rev.* **1957**, *108*, 1164.

(58) Shi, L.; Hao, Q.; Yu, C.; Mingo, N.; Kong, X.; Wang, Z. L. *Appl. Phys. Lett.* **2004**, *84*, 2638.

(59) Türkes, P.; Pluntke, Ch.; Helbig, R. *J. Phys. C: Solid State Phys.* **1980**, *13*, 4941.

(60) Mingo, N. *Phys. Rev. B* **2003**, *68*, 113308.

(61) Callaway, J. *Phys. Rev.* **1959**, *113*, 1046.

(62) Holland, M. G. *Phys. Rev.* **1963**, *113*, 2461.

(63) Li, D.; Wu, Y.; Kim, P.; Shi, L.; Yang, P.; Majumdar, A. *Appl. Phys. Lett.* **2003**, *83*, 2934.

(64) Mingo, N.; Yang, L.; Li, D.; Majumdar, A. *Nano Lett.* **2003**, *3*, 1713.

(65) Morrison, S. R. *Chemical Sensors*, *in Semiconductor Sensors*; John Wiley and Sons: New York, 1994.

(66) Ruhland, B.; Becker, Th.; Muller, G. *Sens. Actuators B* **1998**, *50*, 85.

(67) Shimizu Y.; Egashira, M. *MRS Bull.* **1999**, *24*, 18.

(68) Comini, E.; Faglia, G.; Sberveglieri, G.; Pan, Z. W.; Wang, Z. L. *Appl. Phys. Lett.* **2002**, *81*, 1869.

(69) Oh, S. W.; Kim, Y. H.; Yoo, D. J.; Oh, S. M.; Park, S. J. *Sens. Actuators B* **1993**, *13*, 400.

(70) Kim, C. S.; Lad, R. J.; Tripp, C. P. *Sens. Actuators B* **2001**, *76*, 442.

(71) Jorio, A.; Saito, R.; Hafner, J. H.; Lieber, C. M.; Hunter, M.; McClure, T.; Dresselhaus, G.; Dresselhaus, M. S. *Phys. Rev. Lett.* **2001**, *86*, 1118.

(72) Sfeir, M. Y.; Wang, F.; Huang, L.; Chuang C.-C., Hone, J.; O'Brien, S. P.; Heinz, T. F.; Brus, L. E. *Science* **2004**, *306*, 1540.

(73) Yu, M. F.; Lourie, O.; Dyer, M. J.; Moloni, K.; Kelly, T. F.; Ruoff, R. S. *Science* **2000**, *287*, 637.

(74) Polvani, D. A.; Meng, J. F.; Shekar, N. V. C.; Sharp, J.; Badding, J. V.; *Chem. Mater.* **2001**, *13*, 2068.

(75) Liu, L.; Jayanthi, C. S.; Tang, M. J.; Wu, S. Y.; Tombler, T. W.; Zhou, C. W.; Alexseyev, L.; Kong, J.; Dai, H., *J. Phys. Rev. Lett.* **2000**, *84*, 4950.

(76) Tao, A.; Kim, F.; Hess, C.; Goldberger, J.; He, R.; Sun, Y.; Xia, Y.; Yang, P. *Nano Lett.* **2003**, *3*, 1229.

(77) Whang, D.; Jin, S.; Wu, Y.; Lieber, C. M. *Nano Lett.* **2003**, *3*, 1255.